SCIENCE CHINA
Information Sciences

• RESEARCH PAPER •

March 2024, Vol. 67, Iss. 3, 132401:1–132401:8
https://doi.org/10.1007/s11432-023-3812-1

High-performance broadband photodetector based on $PtSe_2/MoS_2$ heterojunction from visible to near-infrared region

Bin WANG[1,3†], Jian YUAN[2,4†], Mengqi CHE[1,3], Mingxiu LIU[1,3], Yuting ZOU[1,3], Junru AN[1,3], Fan TAN[1,3], Yaru SHI[1,3], Nan ZHANG[1,3], Liujian QI[1,3] & Shaojuan LI[1,3*]

[1]*State Key Laboratory of Luminescence and Applications, Changchun Institute of Optics, Fine Mechanics and Physics, Chinese Academy of Sciences, Changchun* 130033, *China;*
[2]*State Key Laboratory of Applied Optics, Changchun Institute of Optics, Fine Mechanics and Physics, Chinese Academy of Sciences, Changchun* 130033, *China;*
[3]*University of Chinese Academy of Sciences, Beijing* 100049, *China;*
[4]*School of Physics and Electronic Information, Huaibei Normal University, Huaibei* 235000, *China*

Received 27 March 2023/Revised 15 May 2023/Accepted 23 June 2023/Published online 19 February 2024

Abstract Broadband photodetectors based on narrow bandgap 2D materials have garnered considerable interest for application in the field of optoelectronic devices. However, their large dark current hinders device performance. In this work, a $PtSe_2/MoS_2$ heterojunction was fabricated for a broadband photodetector operating within the range of visible to near-infrared. The device exhibited suppressed dark currents with a high rectification ratio of 10^4. The built-in electric field of the heterojunction promoted carrier separation effectively, and the device achieved excellent photoelectric performance with responsivities of 1.7×10^3, 27.52, and 21 mA/W at 635, 785, and 1550 nm wavelengths, respectively. Moreover, the specific detectivities (D^*) were 2.2×10^{13} Jones (635 nm), 3.55×10^{11} Jones (785 nm), and 2.72×10^8 Jones (1550 nm). The device demonstrated a rise/fall time of 131/241 μs under 1550 nm laser illumination. Visible and near-infrared imaging detection was also demonstrated based on the heterojunction device at room temperature. This work sheds light on the remarkable potential of $PtSe_2/MoS_2$ heterojunctions in the domain of high-performance broadband photodetectors.

Keywords photodetector, $PtSe_2/MoS_2$, heterojunction, visible to near infrared, high performance

1 Introduction

Photodetectors play a crucial role in optoelectronic applications, finding wide-ranging applications in optical communication, infrared imaging, spectral analysis, environmental monitoring, and aerospace remote control. At present, the necessity for detectors with capabilities such as high performance, broad spectrum, multiband, and uncooled functionalities is experiencing considerable growth. In particular, achieving high-performance photodetection across a broadband spectral range holds remarkable application value [1–5]. Recently, research on two-dimensional (2D) material-based photodetectors has attracted considerable attention due to the distinctive optoelectronic properties of 2D materials, such as tunable bandgap, high carrier mobility, strong light-matter interaction, and excellent mechanical flexibility [6–8]. For broadband photodetection, 2D materials, such as graphene, black phosphorus, tellurium, and transition-metal dichalcogenides (TMDs), have been implemented in the fabrication of next-generation high-performance broadband photodetectors. Moreover, the detection spectrum ranging from ultraviolet, visible, and infrared to terahertz has been achieved in these broadband 2D photodetectors [9–16]. As an emerging 2D material of group-10 TMDs, $PtSe_2$ has been demonstrated to possess excellent electrical and optoelectrical properties, such as high carrier mobility at room temperature, layer-dependent tunable bandgap, and high stability in the air [17]. In particular, the unique broadband gap

* Corresponding author (email: lishaojuan@ciomp.ac.cn)
† Wang B and Yuan J have the same contribution to this work.

range of $PtSe_2$ makes it an excellent candidate for fabricating broadband visible to infrared photodetectors [18–20]. However, $PtSe_2$ photodetectors, which operate in a photoconductive mode, are limited by high dark current, resulting in relatively low responsivity and slow response speed [21,22], hindering their practical applications in high-performance broadband photodetection. Constructing a van der Waals heterojunction can effectively suppress dark current and improve the responsivity and response speed of the photodetectors due to the built-in electric field generated at the interface of the heterojunction leading to the fast separation and transmission of the photogenerated carriers [23–25]. MoS_2-based photodetectors have shown remarkable performance in the visible region. However, their large bandgap precludes their photodetection in the near-infrared spectral range [26–28]. Thus, combining the advantages of $PtSe_2$ and MoS_2, constructing a $PtSe_2/MoS_2$ heterojunction may not only overcome the problem of high dark current in $PtSe_2$ photodetectors but also expand the photodetection range of MoS_2 photodetectors, leading to high-performance broadband photodetection.

Herein, a high-performance broadband photodetector is fabricated based on the $PtSe_2/MoS_2$ heterojunction. The device exhibits a suppressed dark current, and the built-in electric field promotes charge transfer at the $PtSe_2/MoS_2$ interface. A high current rectification ratio of 10^4 is achieved at room temperature. The device exhibits broadband photodetection capability from the visible to the near-infrared region and demonstrates high responsivities of 1.7×10^3, 27.52, and 21 mA/W under 635, 785, and 1550 nm laser illumination, respectively. Detectivities of 2.2×10^{13} Jones (635 nm), 3.55×10^{11} Jones (785 nm), and 2.72×10^8 Jones (1550 nm) are achieved, revealing the broadband photodetection capability of the device. The response speeds are calculated to be 131 and 241 μs for the rise/fall times, respectively, under a laser illumination of 1550 nm. In addition, an imaging experiment is conducted to verify the broadband imaging capability of the $PtSe_2/MoS_2$ heterojunction photodetector. The findings reveal that the $PtSe_2/MoS_2$ heterojunction has great potential for broadband photodetection and imaging systems.

2 Results and discussion

Figure 1(a) illustrates the optical image of the $PtSe_2/MoS_2$ heterojunction photodetector. The device is constructed in a way that the Si/SiO_2 substrate, 2D $PtSe_2$ film, MoS_2 flake, and metal electrodes (10 nm Ti/80 nm Au) are overlapped from bottom to top. In this work, the 2D $PtSe_2$ film, which is grown by direct selenization of the Pt substrate using the Se source with an ambient pressure conversion process, was synthesized on a 300 nm SiO_2/Si substrate by chemical vapor deposition. The detailed experimental procedures can be seen in the Experiment Section (Supporting information, Figure S1). To further reveal the components and binding energies of the $PtSe_2$ film, the elemental binding energies of $PtSe_2$ were estimated by X-ray photoelectron spectroscopy, and the corresponding spectra are exhibited in Figures S2(a) and (b). In the Pt 4f spectrum, two peaks at 73.9 and 77.3 eV are observed, assigned to Pt $4f_{7/2}$ and Pt $4f_{5/2}$, respectively, confirming the presence of Pt. In addition, the peak positions at 54.39 and 55.19 eV correspond to the binding energy of Se 3d orbitals of divalent selenium ions [29,30]. Energy dispersive X-ray spectroscopy measurement was also conducted to check the uniformity of the $PtSe_2$ film. The elemental mappings of Pt and Se, as shown in Figure S2(c), confirm that both elements are homogeneously distributed throughout the entire structure.

The height profile of the $PtSe_2/MoS_2$ heterojunction is shown in Figure 1(b). The thicknesses of the 2D $PtSe_2$ film and MoS_2 flake are 8.3 and 83 nm, respectively. The atomic force microscopy (AFM) image of the device is shown in the inset (Figure 1(b)). The red line in the inset represents the area where the thickness of the heterojunction is obtained. The Raman spectrum was collected to further characterize the $PtSe_2/MoS_2$ heterojunction and is shown in Figure 1(c). The feature peaks of 176 and 210 cm^{-1} are assigned to the E_g and A_{1g} vibration modes of $PtSe_2$, respectively [18], while the characteristic peaks of MoS_2 are 387 and 408 cm^{-1}, corresponding to the E^1_{2g} and A_{1g} vibration modes, respectively [31]. In addition, all the Raman characteristic peaks of both $PtSe_2$ and MoS_2 can be clearly observed in the overlapped region, signifying that the heterojunction region can reflect the characteristics of the two materials simultaneously. Raman mapping images at 176, 210, 387, and 408 cm^{-1} feature peaks are shown in Figure S3, which shows the good quality of each component in the heterojunction. Furthermore, Figure S4 exhibits the absorption spectrum of $PtSe_2/MoS_2$ heterojunction. Combined with the absorption properties of $PtSe_2$ and MoS_2, the $PtSe_2/MoS_2$ heterojunction exhibits excellent broadband absorption ability from the visible to near-infrared region.

Before exploring the photoelectric properties of the $PtSe_2/MoS_2$ heterojunction photodetector, the

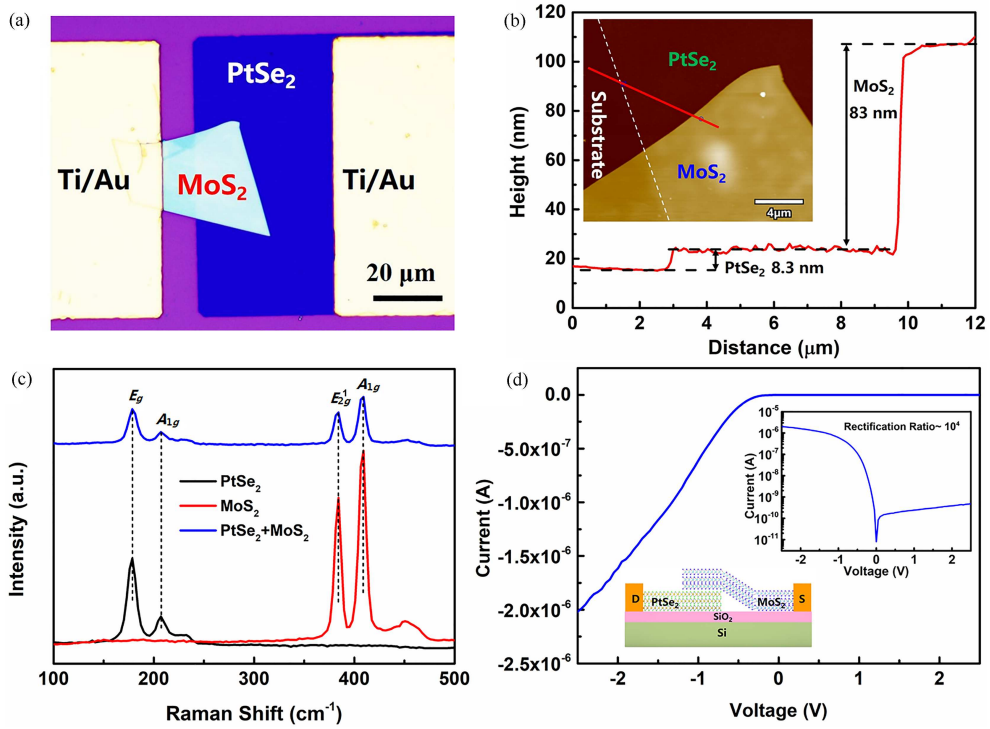

Figure 1 (Color online) (a) Optical image of the $PtSe_2/MoS_2$ heterojunction photodetector. Scale bar: 20 μm. (b) Height profile of the $PtSe_2/MoS_2$ heterojunction; inset is the AFM image. Scale bar: 4 μm. (c) Raman spectra of $PtSe_2$, MoS_2, and $PtSe_2/MoS_2$ heterojunction regions. (d) *I*-*V* linear and log plots (inset) of the $PtSe_2/MoS_2$ heterojunction photodetector in the dark; the inset is the schematic image of the device.

current-voltage (*I*-*V*) characteristics of the device were investigated in the dark and at room temperature using a Keithley 4200 analyzer. The *I*-*V* curves of the individual MoS_2 and $PtSe_2$ devices in the dark are illustrated in Figure S5. The typical ohmic nature of the *I*-*V* curves demonstrates the formation of ohmic contacts between the active material and the Ti/Au electrodes. However, for the $PtSe_2/MoS_2$ heterojunction photodetector, very clear rectification characteristics are observed from the *I*-*V* curve, with a rectification ratio of 10^4 at ±2.5 V (Figure 1(d), inset). This indicates that a heterojunction with a high-quality interface is formed between MoS_2 and $PtSe_2$, and the rectification effect is due to the built-in electric field formed between the $PtSe_2/MoS_2$ heterojunction [32,33]. The schematic view of the $PtSe_2/MoS_2$ heterojunction photodetector is shown as the inset image in Figure 1(d).

Subsequently, the photoelectric properties of the $PtSe_2/MoS_2$ heterojunction photodetector were estimated. Figure 2(a) plots the *I*-*V* curves of the $PtSe_2/MoS_2$ device under a laser illumination of 635 nm with different intensities. Apparently, the current increased gradually with increasing light intensity under the negative drain voltage, which is attributable to the increased number of photocarriers at higher light intensities. To evaluate the photoresponse performance of the $PtSe_2/MoS_2$ device more quantitatively, the responsivity and specific detectivity (D^*) were calculated using the following equations [34,35]:

$$R = \frac{I_p - I_d}{P \times S}, \tag{1}$$

$$D* = \frac{R}{\sqrt{2qJ_d}} = \frac{\sqrt{S} \times R}{\sqrt{2qI_d}}, \tag{2}$$

where R is the responsivity, I_p is the light current, I_d is the dark current, P is the incident laser power density (the diameter of the laser spot is 100 μm), q is the elementary charge, and S is the effective working area of the device (472 μm^2). The responsivity and D^* of the $PtSe_2/MoS_2$ heterojunction photodetector under 635 nm laser illumination with different intensities are shown in Figure 2(b). It is noted that both responsivity and D^* decrease with increasing light intensity, consistent with the behaviors of other reported TMD-based heterojunctions [36,37]. The highest responsivity reaches 1.7×10^3 A/W at $V_{ds} = -2$ V (Figure 2(b), blue curve), while the highest D^* reaches 2.2×10^{13} Jones (1 Jones = 1 cm·$Hz^{1/2}$·W^{-1}) at $V_{ds} = -2$ V (Figure 2(b), red curve).

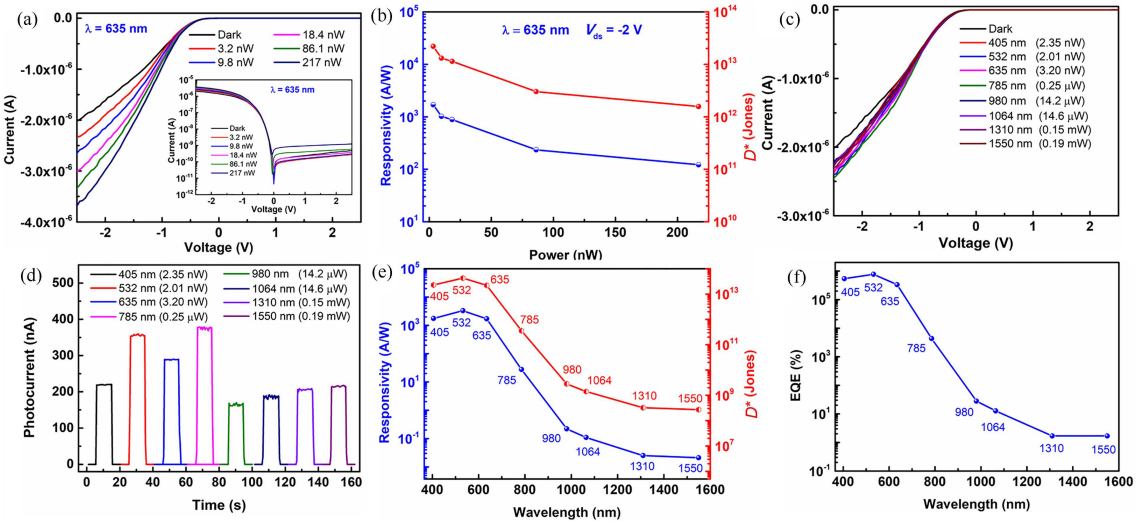

Figure 2 (Color online) (a) I-V curves of the $PtSe_2/MoS_2$ device under 635 nm laser illumination with various intensities. The inset shows the log plots. (b) Responsivity and D^* of the $PtSe_2/MoS_2$ device as a function of laser illumination intensity (635 nm, $V_{ds} = -2$ V). (c) I-V curves of the $PtSe_2/MoS_2$ device under laser illumination with different wavelengths. (d) Time-dependent photocurrent response under laser illumination with different wavelengths ($V_{ds} = -2$ V). (e) Responsivity, D^*, and (f) EQE of the $PtSe_2/MoS_2$ device as a function of laser wavelength ($V_{ds} = -2$ V).

To demonstrate the broadband optical detection capability, the photoelectric properties of $PtSe_2/MoS_2$ heterojunction photodetector under laser illumination with different wavelengths were investigated. In Figure 2(c), the device exhibits an obvious photoresponse under 405, 532, 635, 785, 980, 1064, 1310, and 1550 nm laser illumination, revealing the device's good capability for broadband photodetection from the visible to near-infrared region. The power-dependent I-V curves of the device under laser illumination with different wavelengths are shown in Figures S6 and S7, exhibiting increased light current with increasing laser power. The real-time photoresponse characteristics (I-T) of the device under laser illumination of various wavelengths at -2 V were also explored, as depicted in Figure 2(d). The photocurrent is defined as the difference between the illumination current and the dark current. Also, the unabridged I-T curves under the same test conditions are also exhibited in Figure S8, indicating the stable and repeatable photoresponse of the device. The results show that the $PtSe_2/MoS_2$ heterojunction photodetector exhibits a broadband and stable photosensitivity from the visible (405 nm) to near infrared (1550 nm) region. In addition, the long-term stability of the $PtSe_2/MoS_2$ heterojunction photodetector was investigated. In Figure S9, the currents of the $PtSe_2/MoS_2$ heterojunction photodetector under dark and light (635 and 1550 nm) are almost consistent after 15 days, showing the good stability of the device in the air at room temperature.

To further investigate the broadband detection performance of the $PtSe_2/MoS_2$ heterojunction photodetector, the wavelength-correlated responsivity and D^* were also calculated ($V_{ds} = -2$ V), as shown in Figure 2(e). The responsivity and D^* reach the maximum value of 3.29×10^3 A/W and 4.25×10^{13} Jones under 532 nm laser illumination and 27.52 A/W and 3.55×10^{11} Jones under 785 nm laser illumination, respectively. Moreover, under near-infrared illumination at optical telecommunication wavelengths of 1310 nm (O band) and 1550 nm (C band), the responsivity values are calculated to be 0.025 and 0.021 A/W, and the D^* values are calculated to be 3.23×10^8 and 2.72×10^8 Jones, respectively. Obviously, the $PtSe_2/MoS_2$ heterojunction photodetector shows a broadband photoresponse from the visible to the near-infrared range, even though its responses decrease at optical telecommunication wavelengths. The power-dependent responsivity and D^* of each wavelength (405, 532, 785, 980, 1064, 1310, and 1550 nm) are given in Figures S10 and S11. Furthermore, the external quantum efficiency (EQE) of the $PtSe_2/MoS_2$ heterojunction photodetector, which refers to the number of collected charge carriers per incident photon, is calculated using measured photocurrents and incident laser power densities as follows [38, 39]:

$$\mathrm{EQE} = \frac{I_p/q}{P/h\nu} = R\frac{hc}{\lambda q}, \tag{3}$$

where h and c are the Planck constant and speed of light, λ is the wavelength of laser illumination, R is the responsivity, and q is the elementary charge. Figure 2(f) shows the wavelength-correlated EQE

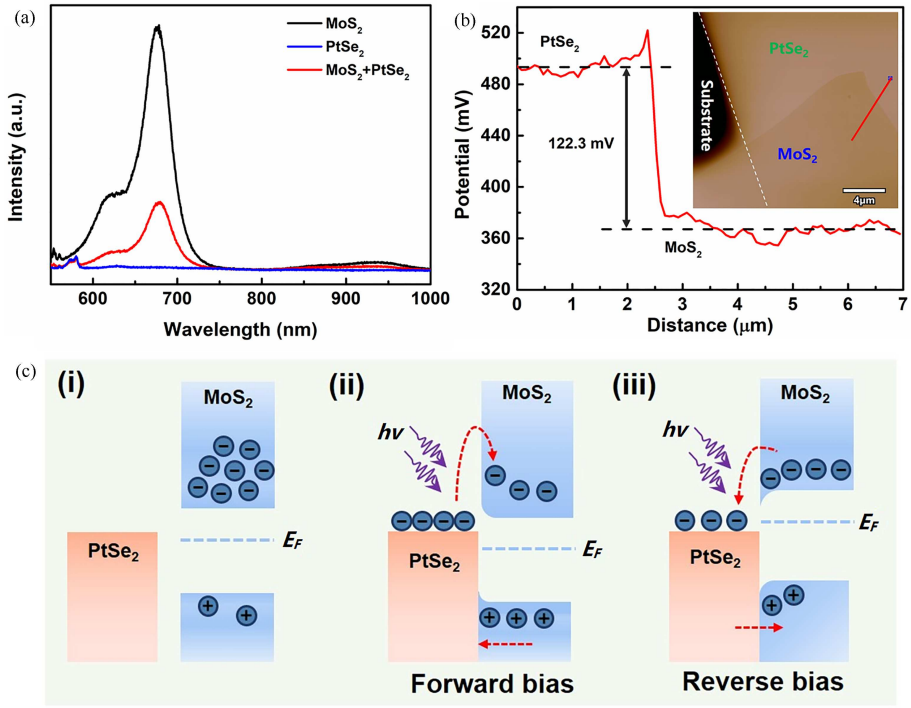

Figure 3 (Color online) (a) Steady-state PL (532 nm excitation) spectra of $PtSe_2$, MoS_2, and $PtSe_2/MoS_2$ heterojunction. (b) Surface potential of the $PtSe_2/MoS_2$ heterojunction (the inset shows the surface potential under illumination; the scale bar is 4 μm). (c) Energy band diagram of the $PtSe_2/MoS_2$ heterojunction photodetector.

($V_{ds} = -2$ V). The calculated EQEs are 7.69×10^5% at 532 nm, 4.36×10^3% at 785 nm, and 1.69% at 1550 nm. The power-dependent EQEs of the wavelengths (405, 532, 635, 785, 980, 1064, 1310, and 1550 nm) are given in Figures S12 and S13. All the above results exhibit the outstanding performance of the $PtSe_2/MoS_2$ heterojunction photodetector, and a summary of the state-of-the-art research on the performances of published $PtSe_2$-based photodetectors is listed in Table S1.

To further understand the photoresponse mechanism of the $PtSe_2/MoS_2$ device under light irradiation, the carrier transport process and energy band diagrams of the $PtSe_2/MoS_2$ heterojunction photodetector were systematically analyzed. Figure 3(a) presents the steady-state photoluminescence (PL) spectra of $PtSe_2$, MoS_2, and $PtSe_2/MoS_2$ heterojunction under an excitation of 532 nm. The PL intensity of the $PtSe_2/MoS_2$ heterojunction shows clear quenching compared to that of MoS_2. The quenching in the steady-state PL is attributed to the reduced carrier recombination rate and enhanced charge separation, which is related to the surface potential at the $PtSe_2/MoS_2$ interface [28, 38, 40]. Kelvin probe force microscopy (KPFM) was also performed to evaluate the surface potential difference at the $PtSe_2/MoS_2$ interface. Figure 3(b) displays the representative KPFM image (inset) and the extracted surface potential curve of the $PtSe_2/MoS_2$ heterojunction. The corresponding surface potential is obtained by scanning along the red line (Figure 3(b) inset). It is observed that the $PtSe_2$ possesses a higher surface potential than the MoS_2 film; the surface potential difference between the $PtSe_2$ and MoS_2 interface is 122.3 mV. The surface potential difference accelerates the transportation of carriers at the $PtSe_2/MoS_2$ interface, characterized by the PL intensity quenching of the $PtSe_2/MoS_2$ heterojunction (Figure 3(a)).

Figure 3(c) shows the energy band diagrams of the $PtSe_2/MoS_2$ heterojunction photodetector. Based on previous studies, the 2D multilayered $PtSe_2$ film can be considered as a semimetal, and the Fermi level (E_F) is located at −4.84 eV [41, 42]. For MoS_2, the conduction band minimum (E_C) and valence band maximum (E_V) are located at −4.3 and −5.5 eV, respectively [28, 43]. The difference in E_F between semimetal $PtSe_2$ and MoS_2 results in the electron transfer from the $PtSe_2$ side to the MoS_2 until both E_F align, leading to a strong built-in electric field across the depletion region. The electrons and holes are then rapidly separated by the built-in electric field and collected by the respective electrodes, ultimately generating current [44–46]. Under the forward bias, the external electric field compensates for the built-in electric field, which narrows the depletion region and increases the current. However, under the reverse bias, the external electric field has the same direction as that of the built-in electric field, which can

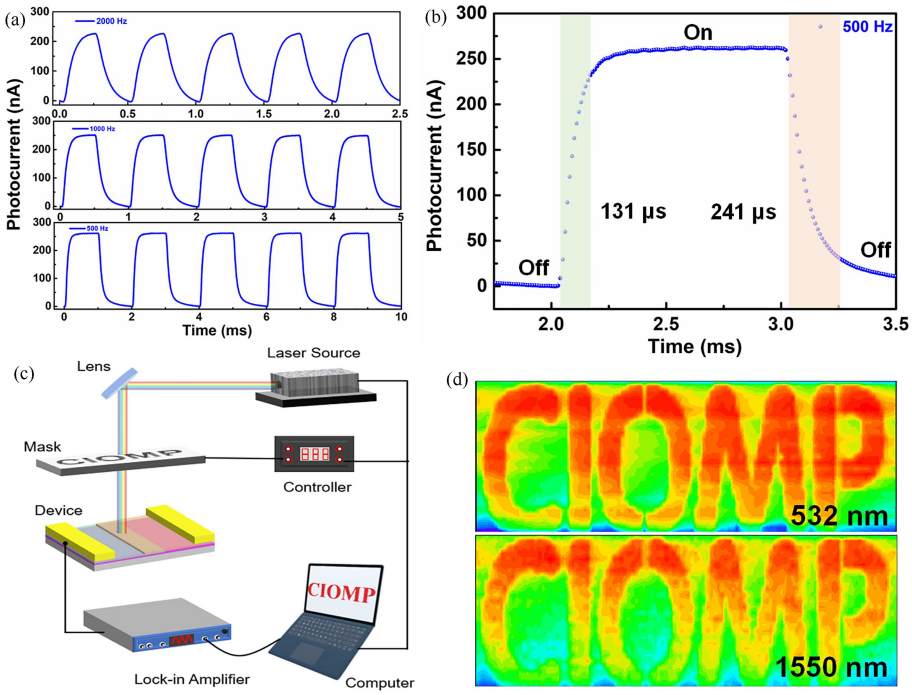

Figure 4 (Color online) (a) Photoresponse properties of the $PtSe_2/MoS_2$ heterojunction photodetector at 2000, 1000, and 500 Hz frequencies (1550 nm, $V_{ds} = -2$ V); (b) enlarged single response for estimating the response speeds at 500 Hz (1550 nm, $V_{ds} = -2$ V); (c) schematic diagram of the imaging measurement system; (d) imaging results of the "CIOMP" letters under 532 and 1550 nm laser illumination.

extend the depletion region and decrease the currents displaying current-rectifying characteristics. An increasing laser illumination leads to an increased photoexcited-carrier density, which would lead to an increase of photocurrents under forward bias.

The response speeds and frequency response were investigated to further evaluate the performances of the $PtSe_2/MoS_2$ heterojunction photodetector, as shown in Figures 4(a) and (b). A near-infrared light of 1550 nm was used as the incident light source, which can be driven by a waveform generator with square-pulse signals. Moreover, an oscilloscope was used to record the time-related photocurrents of the device. Figure 4(a) displays the response properties of the $PtSe_2/MoS_2$ heterojunction photodetector at 500, 1000, and 2000 Hz frequencies under -2 V drain voltage. The stable, repeatable, and fast switching responses to the varying near-infrared light signals can be observed at all frequencies. To ensure the authenticity of response time extraction, the response property at 500 Hz frequency was selected to extract the response times, and the enlarged response curve is shown in Figure 4(b). In the time domain, the rise (or fall) time is defined as the time required for the photoresponse to increase (or decrease) from 10% (or 90%) to 90% (or 10%) out of the peak value [19]. As a result, the rise and fall times (τ_r and τ_f) were estimated to be 131 and 241 μs, respectively. Furthermore, the response speeds of the $PtSe_2/MoS_2$ heterojunction photodetector under a laser illumination of 635 and 785 nm were also estimated, and their enlarged response curves at 500 Hz frequency are shown in Figure S14. The response speeds (rise time/fall time) were estimated to be 134/272 μs for 635 nm and 135/352 μs for 785 nm.

In addition, the $PtSe_2/MoS_2$ heterojunction photodetector has proven to be capable of collecting information from images. The broadband imaging performance of the $PtSe_2/MoS_2$ heterojunction photodetector was experimentally tested under both visible and near-infrared laser illumination. As observed in Figure 4(c), a "CIOMP" mask, which can be controlled to move linearly in the X-Y plane, is placed between the device and the laser source. When the laser source illuminates the device by passing through the mask, the position-dependent real-time photocurrent can be recorded by a lock-in amplifier, and the corresponding photocurrent-based images can be produced by a computer. Figure 4(d) shows the photocurrent-based images measured under laser illuminations of 532 and 1550 nm. The images of "CIOMP" can be clearly recognized under both laser illuminations, revealing that the $PtSe_2/MoS_2$ heterojunction photodetector exhibits superior imaging capability and great potential for broadband photodetection and imaging from the visible to near-infrared region.

3 Conclusion

In summary, a high-performance visible-near-infrared broadband photodetector was fabricated based on the $PtSe_2/MoS_2$ heterojunction. The dark current of the heterojunction device was suppressed efficiently, and the built-in electric field at the $PtSe_2/MoS_2$ interface promoted carrier separation, as confirmed by the PL and KPFM measurements. The device exhibited a high current rectification ratio of 10^4 at room temperature and high responsivities of 3.29×10^3, 1.7×10^3, 27.52, and 21 mA/W under 532, 635, 785, and 1550 nm laser illumination, respectively. The detectivities reached 4.25×10^{13} Jones (532 nm), 2.2×10^{13} Jones (635 nm), 3.55×10^{11} Jones (785 nm), and 2.72×10^8 Jones (1550 nm). A fast response time (rise/fall time) of 131/241 μs was calculated under 1550 nm laser illumination. Furthermore, the $PtSe_2/MoS_2$ heterojunction photodetector showed good imaging capability at visible and near-infrared bands. This research reveals that the $PtSe_2/MoS_2$ heterojunction photodetector has great potential for broadband photodetection and imaging.

Acknowledgements This work was supported by National Key Research and Development Program (Grant No. 2021YFA0717-600), National Natural Science Foundation of China (Grant Nos. 62121005, 62022081, 61974099, 62104226, 62204240), Natural Science Foundation of Jilin Province (Grant Nos. 20210101173JC, 20220508030RC), Changchun Key Research and Development Program (Grant No. 21ZY03), and Open Fund of State Key Laboratory of Applied Optics.

Supporting information Figures S1–S14, Table S1. The supporting information is available online at info.scichina.com and link.springer.com. The supporting materials are published as submitted, without typesetting or editing. The responsibility for scientific accuracy and content remains entirely with the authors.

References

1 Lu X W, Sun L, Jiang P, et al. Progress of photodetectors based on the photothermoelectric effect. Adv Mater, 2019, 31: 1902044
2 Zhang C, Luo Y, Maier S A, et al. Recent progress and future opportunities for hot carrier photodetectors: from ultraviolet to infrared bands. Laser Photon Rev, 2022, 16: 2100714
3 Dhanabalan S C, Ponraj J S, Zhang H, et al. Present perspectives of broadband photodetectors based on nanobelts, nanoribbons, nanosheets and the emerging 2D materials. Nanoscale, 2016, 8: 6410–6434
4 Wu C, Wu F M, Hu H Z, et al. Review of self-powered solar-blind photodetectors based on Ga_2O_3. Mater Today Phys, 2022, 28: 100883
5 Cheng Y X, Ye J H, Lai L, et al. Ambipolarity regulation of deep-UV photocurrent by controlling crystalline phases in Ga_2O_3 nanostructure for switchable logic applications. Adv Elect Mater, 2023, 9: 2201216
6 An J R, Zhao X Y, Zhang Y N, et al. Perspectives of 2D materials for optoelectronic integration. Adv Funct Mater, 2021, 32: 2110119
7 An J R, Wang B, Shu C, et al. Research development of 2D materials based photodetectors towards mid-infrared regime. Nano Sel, 2020, 2: 527–540
8 Long M S, Wang P, Fang H H, et al. Progress, challenges, and opportunities for 2D material based photodetectors. Adv Funct Mater, 2018, 29: 1803807
9 Qiu Q X, Huang Z M. Photodetectors of 2D materials from ultraviolet to terahertz waves. Adv Mater, 2021, 33: 2008126
10 Wang H Y, Li Z X, Li D Y, et al. van der Waals integration based on two-dimensional materials for high-performance infrared photodetectors. Adv Funct Mater, 2021, 31: 2103106
11 Geng H J, Yuan D, Yang Z, et al. Graphene van der Waals heterostructures for high-performance photodetectors. J Mater Chem C, 2019, 7: 11056–11067
12 Guan X W, Yu X C, Periyanagounder D, et al. Recent progress in short- to long-wave infrared photodetection using 2D materials and heterostructures. Adv Opt Mater, 2020, 9: 2001708
13 Zha J J, Luo M C, Ye M, et al. Infrared photodetectors based on 2D materials and nanophotonics. Adv Funct Mater, 2022, 32: 2111970
14 Dong Z, Yu W Z, Zhang L B, et al. Highly efficient, ultrabroad $PdSe_2$ phototransistors from visible to terahertz driven by mutiphysical mechanism. ACS Nano, 2021, 15: 20403–20413
15 Chen Y F, Tan C W, Wang Z, et al. Momentum-matching and band-alignment van der Waals heterostructures for high-efficiency infrared photodetection. Sci Adv, 2022, 8: eabq1781
16 Luo Z T, Xu H K, Gao W, et al. High-performance and polarization-sensitive imaging photodetector based on WS_2/Te tunneling heterostructure. Small, 2023, 19: 2207615
17 Ahmad W, Wu J, Zhuang Q D, et al. Research process on photodetectors based on group-10 transition metal dichalcogenides. Small, 2023, 19: 2207641
18 Cao B L, Ye Z M, Yang L, et al. Recent progress in van der Waals 2D $PtSe_2$. Nanotechnology, 2021, 32: 412001
19 Yuan J, Sun T, Hu Z X, et al. Wafer-scale fabrication of two-dimensional $PtS_2/PtSe_2$ heterojunctions for efficient and broad band photodetection. ACS Appl Mater Interface, 2018, 10: 40614–40622
20 Wang Y L, Li L F, Yao W, et al. Monolayer $PtSe_2$, a new semiconducting transition-metal-dichalcogenide, epitaxially grown by direct selenization of Pt. Nano Lett, 2015, 15: 4013–4018
21 Zhang H T, Li H W, Wang F G, et al. $PtSe_2$ field-effect phototransistor with positive and negative photoconductivity. ACS Appl Electron Mater, 2022, 4: 5177–5183
22 Zhao Y D, Qiao J S, Yu Z H, et al. High-electron-mobility and air-stable 2D layered $PtSe_2$ FETs. Adv Mater, 2017, 29: 1604230
23 Liu X, Wang W H, Yang F, et al. Bi_2O_2Se/BP van der Waals heterojunction for high performance broadband photodetector. Sci China Inf Sci, 2021, 64: 140404
24 Lin Z T, Zhu W B, Zeng Y H, et al. Enhanced photodetection range from visible to shortwave infrared light by $ReSe_2/MoTe_2$ van der Waals heterostructure. Nanomaterials, 2022, 12: 2664

25 An J R, Sun T, Wang B, et al. Efficient graphene in-plane homogeneous p-n-p junction based infrared photodetectors with low dark current. Sci China Inf Sci, 2021, 64: 140403
26 Lopez-Sanchez O, Lembke D, Kayci M, et al. Ultrasensitive photodetectors based on monolayer MoS_2. Nat Nanotech, 2013, 8: 497–501
27 Chen Y, Wang X D, Wu G J, et al. High-performance photovoltaic detector based on $MoTe_2/MoS_2$ van der Waals heterostructure. Small, 2018, 14: 1703293
28 Guo T T, Song X F, Wei P F, et al. High-gain MoS_2/Ta_2 $NiSe_5$ heterojunction photodetectors with charge transfer and suppressing dark current. ACS Appl Mater Interface, 2022, 14: 56384–56394
29 Zeng L H, Lin S H, Li Z J, et al. Fast, self-driven, air-stable, and broadband photodetector based on vertically aligned $PtSe_2$/GaAs heterojunction. Adv Funct Mater, 2018, 28: 1705970
30 Zhuo R R, Zeng L H, Yuan H Y, et al. In-situ fabrication of $PtSe_2$/GaN heterojunction for self-powered deep ultraviolet photodetector with ultrahigh current on/off ratio and detectivity. Nano Res, 2018, 12: 183–189
31 Ganatra R, Zhang Q. Few-layer MoS_2: a promising layered semiconductor. ACS Nano, 2014, 8: 4074–4099
32 Ye L, Li H, Chen Z F, et al. Near-infrared photodetector based on MoS_2/black phosphorus heterojunction. ACS Photon, 2016, 3: 692–699
33 Besse R, Wang H, West D, et al. Prediction of effective photoelectron and hole separation in type-I $MoS_2/PtSe_2$ van der Waals junction. J Phys Chem Lett, 2022, 13: 6407–6411
34 Wu C, Wu F M, Ma C, et al. A general strategy to ultrasensitive Ga_2O_3 based self-powered solar-blind photodetectors. Mater Today Phys, 2022, 23: 100643
35 Wu C, Wu F N, Hu H Z, et al. Work function tunable laser induced graphene electrodes for Schottky type solar-blind photodetectors. Appl Phys Lett, 2022, 120: 101102
36 Xue Y Z, Zhang Y P, Liu Y, et al. Scalable production of a few-layer MoS_2/WS_2 vertical heterojunction array and its application for photodetectors. ACS Nano, 2016, 10: 573–580
37 Wang L, Jie J S, Shao Z B, et al. MoS_2/Si heterojunction with vertically standing layered structure for ultrafast, high-detectivity, self-driven visible-near infrared photodetectors. Adv Funct Mater, 2015, 25: 2910–2919
38 Wang B, Zou Y T, Lu H Y, et al. Boosting perovskite photodetector performance in NIR using plasmonic bowtie nanoantenna arrays. Small, 2020, 16: 2001417
39 Shu K X, Gao W, Wan F S, et al. High-performance broadband photodetectors based on n-MoS_2/p-$Ge_{0.9}Sn_{0.1}$ heterojunctions. ACS Appl Electron Mater, 2021, 3: 3218–3225
40 Yuan J T, Najmaei S, Zhang Z H, et al. Photoluminescence quenching and charge transfer in artificial heterostacks of monolayer transition metal dichalcogenides and few-layer black phosphorus. ACS Nano, 2015, 9: 555–563
41 Xie C, Zeng L H, Zhang Z X, et al. High-performance broadband heterojunction photodetectors based on multilayered $PtSe_2$ directly grown on a Si substrate. Nanoscale, 2018, 10: 15285–15293
42 Zhang Z X, Zeng L H, Tong X W, et al. Ultrafast, self-driven, and air-stable photodetectors based on multilayer $PtSe_2$/perovskite heterojunctions. J Phys Chem Lett, 2018, 9: 1185–1194
43 Wu F, Li Q, Wang P, et al. High efficiency and fast van der Waals hetero-photodiodes with a unilateral depletion region. Nat Commun, 2019, 10: 4663
44 Chen Y X, Zhu Q H, Zhu X D, et al. Gate-tunable high-performance broadband phototransistor array of two-dimensional $PtSe_2$ on SOI. Nano Res, 2023, 16: 7559–7567
45 Ye P, Xiao H, Zhu Q H, et al. Si-CMOS-compatible 2D $PtSe_2$-based self-driven photodetector with ultrahigh responsivity and specific detectivity. Sci China Mater, 2022, 66: 193–201
46 Wu D, Zhao Z H, Lu W, et al. Highly sensitive solar-blind deep ultraviolet photodetector based on graphene/$PtSe_2$/β-Ga_2O_3 2D/3D Schottky junction with ultrafast speed. Nano Res, 2021, 14: 1973–1979